An updated viscous flow law for glacier ice

Meghana Ranganathan[a,b,1] **and Brent Minchew**[a]

[a]Department of Earth, Atmospheric and Planetary Sciences, Massachusetts Institute of Technology, Cambridge, MA, USA; [b]School of Earth and Atmospheric Sciences, Georgia Institute of Technology, Atlanta, GA, USA

This manuscript was compiled on June 16, 2023

Glacier flow modulates sea level and is governed by the viscous deformation of ice. Multiple molecular-scale mechanisms facilitate viscous deformation, but it remains unclear how each contributes to glacier-scale deformation and how to represent them in ice-flow models. Here, we present a model of ice deformation that unifies existing estimates of the viscous parameters and provides a framework for estimating their values. We infer from observations the dominant deformation mechanisms in the Antarctic Ice Sheet, showing that, contrary to long-standing assumptions, dislocation creep, with viscous stress exponent $n = 4$, likely dominates in all fast-flowing areas. This increase from the canonical $n = 3$ dramatically alters the climate conditions under which marine ice sheets may become unstable.

glacier flow | Antarctica | rheology | glaciology

1. Introduction

Changes in mass loss rates from ice sheets (the Antarctic Ice Sheet (AIS) and the Greenland Ice Sheet (GrIS)) are the largest sources of uncertainty in projections of sea-level rise (1). Most of this mass loss from the Antarctic Ice Sheet ice sheets occurs through fast-flowing glaciers and ice streams (2–5), which transport ice from the grounded ice sheet to the ocean. Therefore , ice deformation rates govern these changes in mass loss (6). Understanding and modeling the mechanisms that govern ice deformation – among the oldest, most enduring, and most foundational questions in glaciology – are necessary for understanding the evolution of ice sheets and other glaciated areas, reliably projecting sea-level rise, and quantifying the associated uncertainties.

Multiple mechanisms can give rise to ice deformation (7**?**). Their combined effect can be modeled by a composite flow law (*i.e.*, viscous constitutive relation) wherein the total (bulk) deformation rate $\dot{\epsilon}$ is the sum of deformation rates from several different deformation mechanisms. Laboratory studies provide evidence for four primary deformation mechanisms in glacier ice (8–10) Diffusion creep $\dot{\epsilon}_{\rm diff}$, which arises from the diffusion of vacancies in the crystalline lattice. Grain-boundary sliding $\dot{\epsilon}_{\rm gbs}$, which involves the deformation of a lattice in which the movement occurs within grain boundaries. Dislocation creep $\dot{\epsilon}_{\rm dis}$, which entails the motion of defects (dislocations) in the crystalline lattice. Basal sliding $\dot{\epsilon}_{\rm basal}$ that encompasses slip along the basal planes of crystals to accommodate grain-boundary sliding. Most of these mechanisms act in parallel, but the two grain-boundary-sliding mechanisms, $\dot{\epsilon}_{\rm gbs}$ and $\dot{\epsilon}_{\rm basal}$, act in series because they have opposing rate-limiting mechanisms. Thus, the total rate of deformation given by (9) is

$$\dot{\epsilon} = \dot{\epsilon}_{\rm diff} + \left[\frac{1}{\dot{\epsilon}_{\rm basal}} + \frac{1}{\dot{\epsilon}_{\rm gbs}}\right]^{-1} + \dot{\epsilon}_{\rm dis} \qquad [1]$$

where each term on the right-hand side can be modeled with a power-law relation of the form $\dot{\epsilon}_i = A_i(T, d)\tau^{n_i}$, with T representing the absolute ice temperature, d the mean grain size, τ the effective deviatoric stress, and the parameters A_i and n_i the flow-rate parameter and stress exponent, respectively, for the i^{th} deformation mechanism. Here, we define the effective strain rate and effective stress as (the square root of) the second invariant of the respective tensors (e.g., $\tau = \sqrt{\tau_{ij}\tau_{ij}/2}$ where τ_{ij} is the deviatoric stress tensor and summation is implied for repeated indices).

Rather than trying to represent each individual mechanism as in Equation 1, ice sheet models generally incorporate a single power-law relation commonly known as Glen's Flow Law, which defines a relationship between the effective strain rate $\dot{\epsilon}$ and effective deviatoric stress τ such that (11)

$$\dot{\epsilon} = A\tau^n \qquad [2]$$

While the simplicity of Glen's Law is attractive for modeling, uncertainties in the values of A and n arise from the complex rheology of ice (illustrated in Equation 1) and the challenges in calibrating these parameters at scale in glaciers and ice sheets. In particular, lacking a formal parameterization that captures deformational processes and their effects on A and n, ice sheet models use an assumed value of n and values of A calibrated from observations for the assumed n (12–16). The most common assumption is $n = 3$ for all ice flow conditions and all model timesteps. But while the value of $n = 3$ agrees with some studies (e.g. (13)) and has been argued to provide a good fit to data from multiple studies (15), several other studies have inferred values between 1 and 5 based on laboratory experiments (9, 11, 17, 18), in-situ measurements (13, 19), observational studies (20–22), and computational methods (23**?**). Thus, understanding the relative contributions of different

Significance Statement

The rate of ice flow is a primary control on the rate of mass loss from ice sheets and glaciers. Therefore, the model representation for ice flow is of utmost importance in model projections of future ice sheet, glacier, and sea-level change. However, presently the viscous flow law used in ice sheet models is overly simple and unable to capture spatial and temporal variations in ice flow. Here, we present a framework for calculating the ice-viscosity parameters from ice flow conditions, such as stress, ice temperature, and ice crystal size. This framework allows for modeling variations in ice flow in space and time, and can be readily incorporated into ice sheet models to improve model representation of ice flow and improve estimates of future sea level rise.

Both authors conceived of the study and contributed to the model development. M.I.R. performed the experimentation and developed the figures. Both authors contributed to analyzing and interpreting the results. M.I.R. wrote the original draft and both authors revised and edited the final draft.

The authors declare no competing interests.

[1]To whom correspondence should be addressed. E-mail: meghanar@ucar.edu

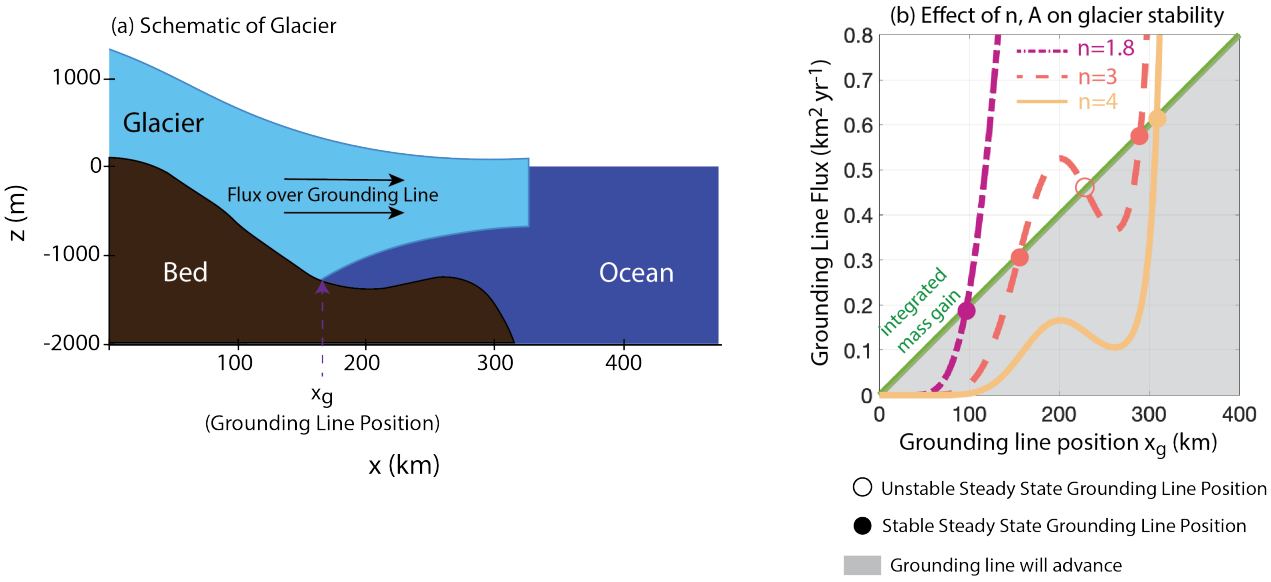

Fig. 1. Effect of n and A on grounding line flux: (a) Schematic of a marine ice sheet, denoting the grounding line position and the flux of ice over the grounding line and into the ocean, a value that affects the mass loss from grounded portions of the ice sheet. The bed geometry is defined in (24). (b) Estimates of the modeled (25) grounding line position (x-axis) and grounding line flux for $n = 2, 3, 4$. Intersections of the green, diagonal line (showing mass flux from surface accumulation integrated over the upstream catchment) with the flux curves are the steady-state grounding line positions, with solid and open circles indicating stable and unstable configurations, respectively. Grey background denotes where the grounding line will advance, and white background denotes where the grounding line will retreat.

deformation mechanisms, and by extension, reasonable values of A and n, remains an open problem that we seek to address in this work.

The assumed values of n and A in ice-flow models have substantial yet, due to the canonical nature of the assumption $n = 3$, largely unexplored implications for ice sheet and sea-level rise projections. The impact arises from the fact that n is the exponent that governs the sensitivity of viscosity to stress, and viscosity is of paramount importance to ice flow (26). In particular, the values of the A and n parameters have profound effects on our conceptualization of the stability of marine ice sheets, like the West Antarctic Ice Sheet, a significant contributor to uncertainties in projections of sea-level rise (1) (Figure 1). Marine ice sheets have beds that are well below sea level and are thought to be unstable when the bed deepens inland (a retrograde slope) because ice floats, allowing for a buoyancy-driven feedback, known as the marine ice sheet instability (MISI), that can cause the rapid retreat of the ice sheet (24, 25, 27, 28).

By definition, MISI can be triggered when the combination of ice rheology and climate allows for an unstable steady state when the grounding line (boundary between grounded and floating ice) is on a retrograde bed slope (Fig. 1b, orange dashed curve) (24). To demonstrate the potential effect of n, A values on ice sheet stability, we apply a simple, steady-state model (25) to a commonly used idealized marine ice sheet geometry (Fig. 1). Our results for $n = 2, 3, 4$, with corresponding values of A taken from the model we describe herein (Fig. 1b), show that varying the viscous parameters within the range of known uncertainties changes the relationship between ice mass flux from land to the ocean (a.k.a., grounding line flux) and grounding line position enough to introduce or eliminate the potential for MISI under given climate scenarios. For the chosen climate scenario, the model shows an unstable grounding line position on the retrograde bed when $n = 3$, but for $n = 2$ and $n = 4$, the grounding line positions are unconditionally stable (Fig. 1b, colored curves). There are no climate scenarios under which a marine ice sheet has an unstable grounding line position for all possible A, n pairs. This simple analysis shows that estimates of marine ice sheet stability and, therefore, sea-level rise projections, are highly sensitive to the values of n and A. This creates an urgent need for more accurate and physically justified estimates of A and n in natural glacier ice and motivates this study, wherein we present a model for ice deformation that represents the salient known mechanisms of ice deformation (Equation 1) and the couplings between ice rheology, temperature, stress, and grain size.

2. A model for n and A in Glen's Flow Law

Our model builds on a series of laboratory experiments (8, 9, 29) that support a composite flow law of the form given in Equation 1 and provide some estimates of the relevant parameters. While the interpretation and details of these studies are still debated in the literature (30–32), the framework for and broad takeaways from our model should be valid as they depend on long-standing principles in the rheology of polycrystalline materials and empirical evidence (33–35). We further discuss assumptions made by this composite flow law in the Discussion section of this paper.

The results from the laboratory studies we build on show that the typical stresses and temperature conditions in ice sheets reduce Equation 1 to the sum of two mechanisms, dislocation creep $\dot{\epsilon}_{\rm dis}$ and grain boundary sliding $\dot{\epsilon}_{\rm gbs}$. This is because diffusion creep ($\dot{\epsilon}_{\rm diff}$) and basal slip-accommodating grain-boundary sliding ($\dot{\epsilon}_{\rm basal}$) are most relevant at lower stresses than are typically found in fast-flowing regions of ice sheets ($\sim 0.1 - 1$ MPa) (8, 9, 29). Therefore, the composite flow law (Equation 1) for active regions of ice sheets

simplifies to

$$\begin{aligned}\dot{\epsilon} &= \dot{\epsilon}_{\text{dis}} + \dot{\epsilon}_{\text{gbs}} \\ &= A_{\text{dis}}(T)\tau^{n_{\text{dis}}} + A_{\text{gbs}}(T)d^{-m}\tau^{n_{\text{gbs}}} \\ &= A_{\text{dis}_0} e^{\frac{-Q_{\text{dis}}}{RT}} \tau^{n_{\text{dis}}} + A_{\text{gbs}_0} d^{-m} e^{\frac{-Q_{\text{gbs}}}{RT}} \tau^{n_{\text{gbs}}}\end{aligned} \quad [3]$$

where Q_i is the activation energy for mechanism i, A_{i_0} is the prefactor for mechanism i, R is the ideal gas constant, $m = 1.4$ (9), and the other factors are defined as in Glen's Flow Law (Equation 2) but for specific deformation mechanisms. We apply this composite flow law to illuminate the spatial variability in Glen's Flow Law parameters (n and A; Equation 2). In practice, this approach may be preferable to incorporating composite flow laws directly into ice-flow models since many of these models incorporate Glen's Flow Law as presented in Equation 2, and using instead the sum of power laws (Equation 3) can complicate the internal workings of ice sheet models. Further, the method presented here obviates the need for modelers to explicitly solve for grain-size, since the grain size model is embedded here within the model for n, A.

The value of the stress exponent n varies based on the creep mechanism, with dislocation creep best parameterized with $n = 4$ and grain-boundary sliding best parameterized with $n = 1.8$ (9, 29). Therefore, the regions where a single mechanism is the dominant contributor to ice deformation can be represented with the respective value of n: Where dislocation creep dominates $n = n_{dis} = 4$ and where grain-boundary sliding dominates $n = n_{gbs} = 1.8$. Where neither mechanism dominates, we expect n to take on an intermediate value $1.8 < n < 4$. The value of the flow-rate parameter A would vary according to the value of n and according to ice temperature and grain size (15).

To compute values of n, we assume that the balance of flow mechanisms (and thus the value of n) vary smootly in stress-temperature space. For a sufficiently small range, this is a reasonable assumption given that the value of n is unlikely to change rapidly with strain rate. Using the scalar form of Glen's Flow Law (Equation 2), we calculate n as the slope

$$n = \frac{\log \dot{\epsilon}_{\text{min}} - \log \dot{\epsilon}_{\text{max}}}{\log \tau_{\text{min}} - \log \tau_{\text{max}}} \quad [4]$$

where $\dot{\epsilon}_{\text{min}} = \dot{\epsilon} - \Delta\dot{\epsilon}$ and $\dot{\epsilon}_{\text{max}} = \dot{\epsilon} + \Delta\dot{\epsilon}$ and we compute τ_{min} and τ_{max} from Equation 3. Here, we use $\Delta\dot{\epsilon} = 10^{-3}\dot{\epsilon}$ to be the range of effective strain rate for which the flow mechanism may remain approximately constant. We show in the supplement that the choice of $\Delta\dot{\epsilon}$ does not significantly affect the results for all values $\Delta\dot{\epsilon} \leq 0.1\dot{\epsilon}$.

We obtain all the relevant pieces of Equation 4 from either observations or physical models. Effective strain rate $\dot{\epsilon}$ is observable from the gradient of surface velocity fields, which are routinely measured from remote sensing observations. To represent the dependence of deformation rate on ice temperature and grain size, the two variables that affect the dominance of the deformation mechanisms, we couple Equation 1 to a thermomechanical model (36) and a steady-state grain size model (37). This allows us to constrain the mechanisms of ice deformation in natural glacier ice and to estimate the viscous properties of ice for the full range of temperatures and stresses found in glaciers and ice sheets on Earth. We then solve for stress from $\dot{\epsilon}, d, T$ using an iterative nonlinear equation solver on Equation 3.

The constitutive models make some critical assumptions, explored in detail in the respective publications and summarized here. First, they assume that temperature and grain size are in steady state. Therefore, the results shown here can be interpreted as constraining the mechanisms by which ice flows under a steady forcing. Secondly, they assume that ice advection is vertical, and therefore horizontal (lateral and along-flow) advection is negligible. We apply this assumption to simplify the advective component of the model. Previous work suggests that our results should be reasonably accurate in Antarctica despite this simplifying assumption (36). We leave adding horizontal advective components into this model framework to future work but note that our calibration of the activation energies (Fig. 2 and Table 1) and the deformation maps (Fig. 3) we present herein, are valid regardless of our assumptions about advection; only the results we show for some grounded regions of Antarctica can be influenced by our decision to neglect horizontal advection, the implications of which have been discussed in detail in previous publications (36, 38, 39). Finally, the ice temperature and grain size models assume that strain-rate is constant with depth, approximating a situation in which the glacier is slipping over soft sediment or the bed is highly lubricated with liquid water. This assumption limits our results in Antarctica to fast-flowing glaciers (38, 40–42), though the broader conclusions for the dependence of n and A on stress and temperature should be valid for areas where much of the surface velocity is attributable to deformation within the ice column (i.e., vertical shearing) because deformation mechanisms do not directly depend on gravity. As far as deformation mechanisms are concerned, we can reasonably assume that vertical shearing is the same as lateral shearing for a given ice temperature.

3. Benchmarking the model

To ensure that our model produces estimates that are compatible with laboratory studies and ice-sheet observations, we use empirical values from laboratory studies to benchmark our model with recent observational studies by (21) and (22). Both of these observational studies estimate the dependence of the deformation rate on stress in relatively slow-deforming regions of ice sheets. (21) studied vertical-shear-dominated regions in the northern part of the Greenland Ice Sheet. (22) considered the regions of Antarctic ice shelves where ice deformation is well approximated as uniaxial extension. These studies estimated $n \approx 4$ (indicating that dislocation creep is dominant) in their study areas. We expect our model to produce the same results in the same areas as in (22) and under similar conditions to (21).

We first apply Equation 4 to estimate n using the models for ice temperature and grain size described above and the "laboratory" values for the flow law parameters (denoted by a black star in Figure 2a; values presented in Table 1). Using these laboratory values, in Figure 2b(i), we calculate n for varying temperatures and stresses and present where the region studied in (21) would lie in temperature-stress space, and in Figure 2c(i), we show estimates of n in one of the regions studied by (22). In both cases, we find that our estimates of n are inconsistent with those inferred from observations by (21) and (22). For the stresses likely applicable to the interior

of the Greenland ice Sheet (Figure 2b(i)), using laboratory parameters produces estimates of $n \approx 2$, rather than the $n = 4$ as bounf by (21). Similarly, when applying Equation 4 to the Ross Ice Shelf, we find $n \approx 3$, rather than $n = 4$ as found by (22).

There are numerous uncertainties within the model for n that may lead to this discrepancy. These include the choice of model for ice temperature and grain size, the values of n_{dis} and n_{gbs}, and the parameters within A_{dis} and A_{gbs} (the prefactor A_0 and activation energy Q for each mechanism). We propose that the mismatch of our model results and those of observational studies may come from minor errors in the activation energy values used in our model, and we will discuss the justification for this choice below.

To demonstrate the sensitivity of n to activation energy values, we calculate n for varying grain-boundary sliding and dislocation creep activation energies (Figure 2a). In this idealized set-up, we let $\dot{\epsilon} = 10^{-10}$ s^{-1} and $T = 250$ K, and therefore we only vary the low-temperature activation energy value. The laboratory values are denoted by the black star. Estimates of n vary significantly based on values of low-temperature activation energy. In general, $n \approx 2$ for low values of Q^-_{gbs} and high values of Q^-_{dis} and $n \approx 4$ for high values of Q^-_{gbs} and low values of Q^-_{dis}.

The sensitivity to activation energy in particular is expected given the principles of kinetics. When activation energies for dislocation creep are large, deformation by dislocation creep will require more thermal energy, by definition. Similarly, when activation energies for grain-boundary sliding are large, deformation by grain-boundary sliding will require more energy. There is a clear boundary between $n \approx 2$ and $n \approx 4$, in which $2.5 < n < 3.5$ for some combinations of Q^-_{gbs} and Q^-_{dis}. The laboratory values of low-temperature activation energies lie on one edge of this boundary, such that, with very minor deviations from these laboratory values, the estimated n value may change significantly because a different disclocation mechanism becomes more energetically favorable.

This nonlinear response of n to changes in parameter values is not likely the case for uncertainties in the other flow law parameters, such as the exponents n_{gbs} and n_{dis} and the prefactors A_0 (43). In particular, the value of n is significantly more sensitive to activation energy than the prefactors A_0, due to the exponential dependence of activation energy on the deformation rate from a particular deformation mechanism. We show further in the supplement that the value of n is quite insensitive to the values of the prefactors A_0.

As shown in Figure 2b(i), the estimates of n are less sensitive to the choice of temperature (and therefore, grain size) at a given stress state, with the exception of a very narrow range of stresses and temperatures from $10 - 60$ kPa and $260 - 265$ K. We show in the supplement that the grain size primarily affects the estimated n value at high temperatures $T > 263$ K (which are not likely in the regions that (21, 22) studied).

As a summary, the values of activation energy appear to dictate the stress at which the transition from $n \approx 2$ and $n \approx 4$ occurs (e.g. Figure 2b(i)), making n uniquely sensitive to activation energy. Therefore, minor adjustments of the activation energy values (well within laboratory uncertainty) can result in values of n that align with observations (21, 22). For the other uncertain parameters (values of $n_i, A_{0_i},$, temperature, and grain size), very significant deviations in the values would have to be implemented to produce values of n that align with observations.

Table 1. Rheological parameters for dislocation creep and grain-boundary sliding. Laboratory values are from (9, 45).

Parameter	Laboratory Value	Recalibrated Value	Unit
$A^+_{0_{\text{dis}}}$	6.96×10^{23}	6.96×10^{23}	MPa$^{-n_{\text{dis}}}$ s^{-1}
$A^-_{0_{\text{dis}}}$	5×10^5	5×10^5	MPa$^{-n_{\text{dis}}}$ s^{-1}
Q^+_{dis}	155×10^3	151×10^3	J mol^{-1}
Q^-_{dis}	64×10^3	60×10^3	J mol^{-1}
$A^+_{0_{\text{gbs}}}$	8.5×10^{37}	8.5×10^{37}	MPa$^{-n_{\text{gbs}}}$ m^m s^{-1}
$A^-_{0_{\text{gbs}}}$	1.1×10^2	1.1×10^2	MPa$^{-n_{\text{gbs}}}$ m^m s^{-1}
Q^+_{gbs}	250×10^3	255×10^3	J mol^{-1}
Q^-_{gbs}	70×10^3	75×10^3	J mol^{-1}

To ensure consistency with observations, we propose a recalibration of the low-temperature activation energy values to calculate $n \approx 4$ in conditions similar to those studied in (21) and (22), while minimizing deviations from the laboratory values. We choose $Q^-_{\text{gbs}} = 75$ kJ mol^{-1} and $Q^-_{\text{dis}} = 60$ kJ mol^{-1}, values well within the range of laboratory experiments (44) (and references therein) and denoted by red stars in Fig 2. We recalibrate the high-temperature activation energy values to preserve the relative behaviors in low- and high-temperature deformation. For practical purposes, this means that we adjust the high-temperature values to provide a smooth transition in strain rate in the vicinity of temperature transition from warm to cold activation energies, centered at 263 K (15). The recalibrated parameters are given in Table 1.

It is possible that the inconsistency between observations and our model estimates with the laboratory values comes from some other uncertainties rather than activation energy uncertainties. If this inconsistency is due to non-activation energy uncertainties, the calibration of these activation energy values could be thought of as a model adjustment to make up for those uncertainties, in a similar way that we parameterize the strain-rate acceleration at high temperatures by a discontinuous increase in activation energy around 263 K (15). If this is the case, the recalibration may not improve the accuracy of the activation energy values, but it does improve the agreement between our modeled values of n and those inferred from observations observations, thereby tackling the symptom of the problem, if not the cause. For the remainder of this paper, we use the recalibrated values of activation energy to maintain consistency with ice-sheet observations and laboratory data as much as possible. In the supplement, we present the same results as in Figures 3 and 4 using the laboratory activation energy values.

4. Deformation maps: n and A for varying temperatures and stresses

We estimate the Glen's Flow Law parameters, n and A, for varying stresses and temperatures (and thus, strain rates), and organize the results into deformation maps (Figure 3). As shown in these maps, dislocation creep ($n = 4$) dominates when stresses are above 100 kPa, while grain boundary sliding ($n = 1.8$) dominates at lower stresses (< 10 kPa), as expected from previous studies (8, 9, 29, 46). At intermediate stresses of order 10–100 kPa, a range that encompasses most values of stress found in fast-flowing areas of Antarctica, the dominant creep

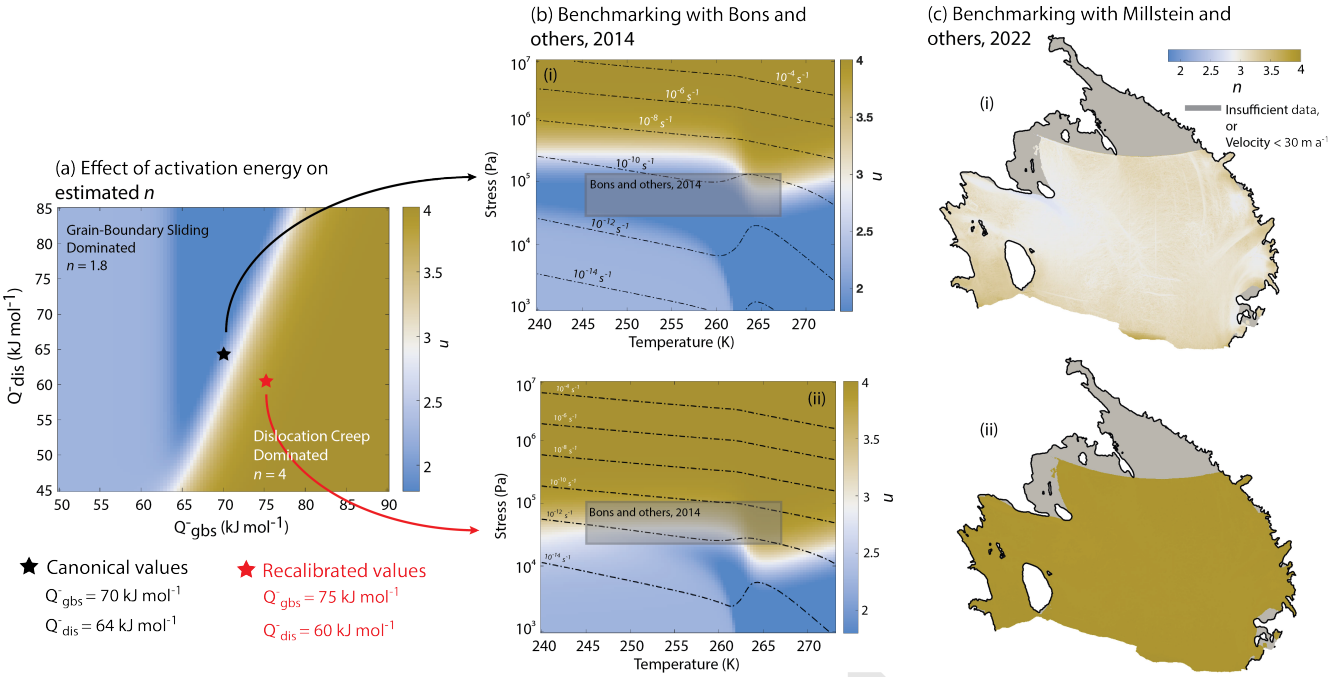

Fig. 2. Benchmarking the model and recalibrating the activation energies: (a) Estimates of n for varying dislocation creep and grain-boundary sliding activation energies. The black star denotes the laboratory values typically used in ice sheet models, and the red star denotes our recalibrated values. (b,c) To recalibrate the values, we benchmark our n estimates against two observational studies: (21) and (22). To do so, we produce estimates of n for (b) similar temperatures and stresses found in the interior of the Greenland Ice Sheet, and (c) the Ross Ice Shelf. We find estimates of $n < 4$ in both cases using the laboratory values (b(i), c(i)), and after recalibration we estimate $n = 4$ in both cases, consistent with observations (b(ii), c(ii)).

mechanism depends strongly on temperature, with dislocation creep ($n = 4$) dominating at warmer temperatures ($263 < T \leq 273$ K), which are expected in rapidly deforming areas (47), and multiple deformation mechanisms acting in concert at colder temperatures. Where both dislocation creep and grain boundary sliding are important, our model gives $n \approx 3$, a narrow region in stress-temperature space that is indicated by the light-colored strip running through the middle of the deformation maps. At stresses below 30 kPa and temperatures colder than 263 K, the estimated value of n is anomalously large due to elevated grain sizes; we do not expect results in these stress-temperature conditions to be realistic nor to impact the primary conclusions of this study because at such low stresses and temperatures, other deformation mechanisms (such as basal slip or diffusion creep) that are not represented in our model may play important roles.

The deformation maps suggest that our model provides a unifying framework for ice viscosity that explains the variations in observational studies from $n \approx 2$ to $n \approx 4$ as a manifestation of measurements being taken at various stresses and ice temperatures. To illustrate this point, we highlight the results of some observational studies with semi-transparent boxes in Fig. 3a. Many of the studies concluding $n = 2 - 3$ have been done in conditions that fall along this boundary between $n \approx 2$ and $n = 4$, with stresses of 10–100 kPa and temperatures < 262 K (e.g. (49) in Byrd Station, Antarctica and Camp Century, Greenland and (50) in Devon Island Ice Cap, Canada). (52) (Taylor Glacier, Antarctica) and (51) (Roosevelt Island, Antarctica) concluded that n may vary between $n = 3$ and $n = 4$. These two studies considered slightly higher stresses and a wider range of ice temperatures, falling between the boundary of $n = 3$ and $n = 4$ in our deformation map. Our estimates are also compatible with studies that conclude $n = 4$. (48) studied a temperate glacier, Athabasca Glacier, and at these high temperatures, we also estimate $n = 4$. Based on tentative estimates of what the ice temperatures may be in these regions, we estimate $n = 3 - 4$ for the same flow conditions.

Applying our estimates of n to Glen's Flow Law, we calculate the prefactor A (Fig. 3b). In regions where $n \approx 4$, we estimate $A \leq 10^{-28}$ $\text{Pa}^{-\text{n}}$ s^{-1}, while where $n \approx 2$, $A > 10^{-20}$ $\text{Pa}^{-\text{n}}$ s^{-1}. Given the difference in exponent, the increase in the magnitude of A for decreasing n is expected because stresses are of order 10^4–10^5 Pa. A is temperature- and grain size-dependent, and therefore as temperature increases, A increases approximately one and a half orders of magnitude. Using this method and with reasonable estimates of n, strain-rate, and applied stress, we can estimate ice viscosity in ice sheets, providing insight into the magnitude of ice softening due to mechanisms such as fabric development, heating, recrystallization, and liquid water content.

5. Estimates of n and A in the Antarctic Ice Sheet

Our model demonstrates how fundamental rheological parameters are affected by ice flow conditions, and it enables estimates of the dominant deformation mechanisms and relevant viscous parameters across AIS. This is possible because ice in Antarctica should be relatively dry; ultimately we will be able to apply the model to wetter ice in Greenland once we better understand how interstitial liquid water content influences the balance of creep mechanisms. Here, we present estimates in AIS with specific focus on Pine Island Glacier, Byrd Glacier,

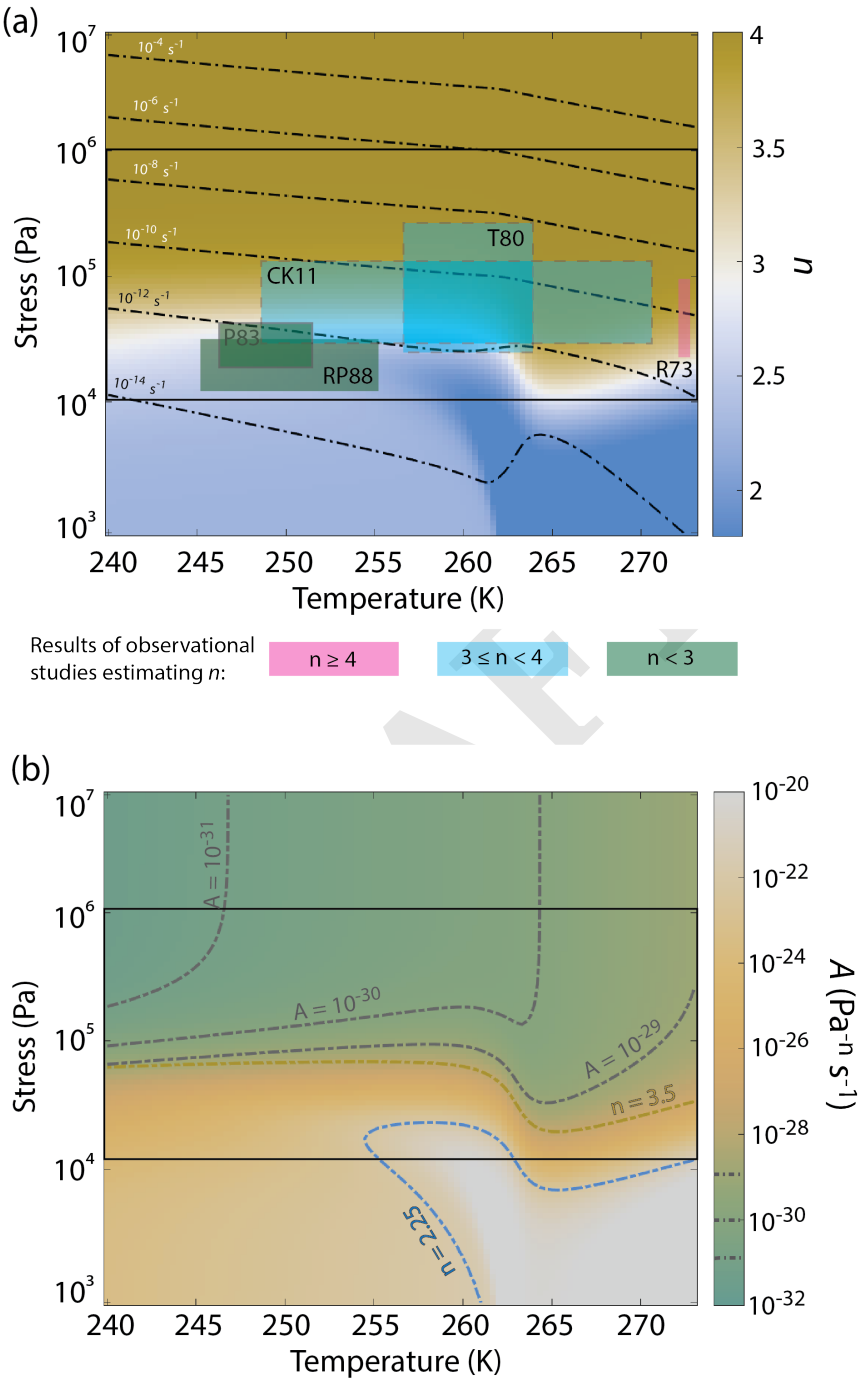

Fig. 3. Estimating $\mathbf{n}$ and $\mathbf{A}$ for varying flow conditions: We estimate for varying stresses and ice temperatures common in naturally-deforming glacier ice: (a) stress exponent in Glen's Flow Law n from our model compared to observational studies, with outlines denoting confidence in the ranges (solid outlines - explicit uncertainties were given in the original study, dashed outlines - enough information was provided in the original study to suggest ranges, no outlines - ranges were inferred by us based on information provided in the original study and knowledge of regions). The labels, which represent author last name and year of publication, and inferred n values are: R73 (48) $n = 4.2$, P83 (49) $n = 2.5 - 3$, RP88 (50) $n = 2.9$, T80 (51) $(n = 3 - 4)$, CK11 (52) $n = 3 - 4$. (b) The flow-rate parameter in Glen's Flow Law A from Equation 2. Contour lines of (a-d) show values of constant strain-rate and red dots show the ice temperatures computed from stress by a thermomechanical model. Contour lines show values of $n = 2.25$ (blue), $n = 3.5$ (gold) and values of A (grey).

Bindschadler and MacAyeal Ice Streams, and Amery Ice Shelf, all of which are well-observed, fast-flowing areas that represent a range of dynamical characteristics. Computing n, A requires observations of effective strain-rates, ice thickness, and surface mass balance. Effective strain-rates are derived from Landsat 7 and 8 velocity fields (3) using methods described in (36). Ice thickness is calculated from basal topography from BedMachine (53) and surface elevation from the Reference Elevation Model of Antarctica (54). Surface mass balance, averaged over 1979-2019, is estimated from RACMO, a regional climate model (55). The estimates presented here are depth-averaged.

We estimate $n \approx 4$ in all fast-flowing areas of AIS (Fig. 4). Within ice streams, the value of n varies slightly around $n = 4$. For example, within Byrd Glacier, the value in the centerline is ~ 3.9. The value of n varies between 3.9 and 4 near the grounding line of Bindschadler and MacAyeal Ice Streams. However, this variance is minimal and $n = 4$ is a good approximation over all of these ice streams.

We further present estimates of A across the AIS and in specific regions of the ice sheet. In Antarctic ice streams, lateral shear is primarily localized in the lateral margins, and thus in our model the margins of ice streams are warmer and expected to have larger grain sizes (37). Both of these processes affect estimates of ice viscosity. Here, we see generally that A is larger in these rapidly-deforming regions of the ice sheet. This result is inline with a number of modeling and computational studies suggesting that ice is warmer and softer in shear margins (38, 58–62).

6. Dependence of Results on Choice of Composite Flow Law

These results depend on some key assumptions about ice flow. Importantly, they depend on the assumption that dislocation creep and grain-boundary sliding are both active in ice sheets, that the contributions of these two mechanisms operate independently such that their contributions can be summed according to the composite flow law, and that they are the dominant two mechanisms controlling ice flow in natural conditions. Some studies have suggested that the behavior identified by (9, 29) as grain-boundary sliding may in fact be descriptive of other processes, such as the accommodation of basal slip by grain-boundary migration, which acts as a recovery mechanism (32, 63). While more work needs to be done to determine the physical mechanism behind the $n = 1.8$ regime, the analysis here should be robust to the specific mechanisms that produce the stress dependencies, since this work is interested primarily in determining under which conditions each regime is most applicable. However, uncertainties would be reduced by further investigation into which process is dominant and the incorporation of a physical understanding of that process into the model.

Relatedly, these results are further dependent upon the construction of the composite flow law itself, as presented in (9). Multi-term flow laws have been presented in a number of studies to describe changes in flow mechanisms at varying stresses. These flow laws are all similar in that they are generally constructed such that a term with a lower stress exponent dominates at lower stresses and a term with a higher stress exponent dominates at higher stresses, in agreement with observational and laboratory data (10, 64–66). Many of these multi-term flow laws are empirical or phenomenological, setting up terms that do not explicitly describe physical mechanisms but rather are used to describe a changing nonlinearity of flow with stress (46, 65, 67, 68). Many of these multi-term flow laws have either two or three terms. Those with two terms generally have a linear term and a term with $n = 3$, as in (46). Those with three terms typically have terms with $n = 1, 3, 5$, as in (65, 68). While here we use the composite flow law presented in (9), for future work, other multi-term flow laws could be used in this framework presented in this study to evaluate the range of n estimates for varying flow laws.

Because we focus on the prevalent stresses and temperatures found in existing glaciers and ice sheets, this work does not account for other creep mechanisms such as diffusion creep and basal slip. Further, the composite flow law used here primarily describes dislocation slip on basal planes. This neglects processes that have been identified to be active at high stresses, such as dislocation climb and slip that occurs on non-basal planes (69). While (9) suggests that mechanisms like diffusion creep and basal slip are unlikely to be dominant in naturally deforming ice, more work needs to be done to determine whether we can neglect these mechanisms and still accurately capture ice flow in our models.

Other processes not considered here include the effect of anisotropy. Fabric may increase the rate of ice deformation up to an order of magnitude, due to the development of a crystallographic preferred orientation accommodating basal slip (70–73). Many modeling frameworks suggest that fabric can be parameterized by a strain-rate enhancement factor of $\sim 2 - 10$ (72, 74, 75). This may be a way of incorporating fabric into this modeling framework to consider the effects of fabric development on deformation rates.

While we neglect some of the complexity of ice flow, we believe this study is a step towards understanding the controls of ice flow and identifying the parameters in ice flow models that ought to be further constrained. Additional complexities in the deformation of ice could be incorporated into this framework by altering the composite flow law used.

7. Conclusion

Ultimately, the way we model ice deformation likely has significant effects on projections of glacier behavior, ice-sheet stability, and sea-level rise (Fig. 1). Our model provides physically-informed estimates of the fundamental parameters underlying our representation of viscous ice flow: the stress exponent n and prefactor A in Glen's Flow Law. The practical implications of our model are 1) the unification of ice deformation that captures and contextualizes the range of existing estimates of the stress exponent n and 2) establishment of a framework for estimating the values of A and n in Glen's Flow Law (Equation 2) based on first principles, laboratory experiments, and observations. This modeling framework can be readily applied to existing ice-flow models while respecting the various coupled physical processes, such as internal heating due to deformation and evolving grain sizes, as a way of improving our parameterization of ice deformation and as part of a broader community effort to make more reliable projections of sea-level rise.

We provide a framework for modeling the variability of the viscous flow parameters with realistic stress and temperature conditions, which provides a step towards incorporating in-

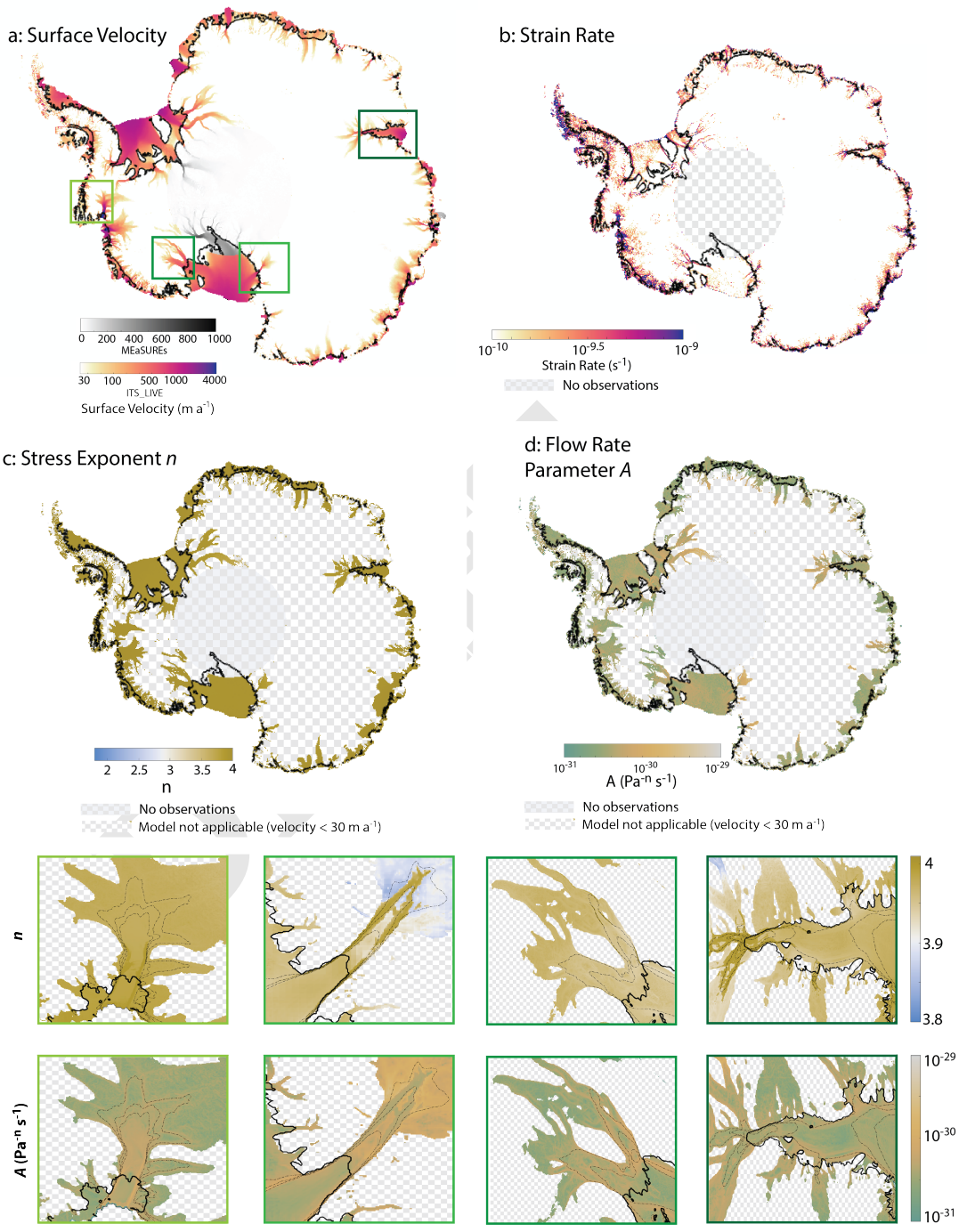

Fig. 4. Estimating $\mathbf{n}$ and $\mathbf{A}$ in regions of the Antarctic Ice Sheet: Using observations of (a) surface velocity (3, 4) and (b) calculated strain-rates (56), we estimate (c) n and (d) A over the Antarctic Ice Sheet. Cross-hatching shows gaps in the data, and greyed out regions are where measured velocity is less than $30\ \mathrm{m\ a^{-1}}$, and our model is not applicable. In the bottom two rows, we show n (upper row) and A (lower row) in (left to right) Pine Island Glacier, Byrd Glacier, Bindschadler and MacAyeal Ice Streams, and the Amery Ice Shelf. Dashed lines denote surface velocity contours of $200\ \mathrm{m\ yr^{-1}}$, $400\ \mathrm{m\ yr^{-1}}$, $600\ \mathrm{m\ yr^{-1}}$. Solid lines denote the grounding line from Bedmap2 (57).

Table 2. Parameters used in the ice temperature model

Parameter	Value	Unit
ρ	917	kg m^{-3}
c_p	2050	J kg^{-1} K^{-1}
a	60 or found from data	mm yr^{-1}
T_m	273	K
K	2.1	W m^{-1} K^{-1}

creased physical complexity into ice flow models with minimal increases in the complexity of the models themselves. Interested readers will find the results shown in the deformation maps (Figure 3) in an hdf5 file in the supplement, which can be used as a simple look-up table in models used for sea-level rise projections. Such a framework should bolster the physical underpinnings of models used to project sea-level and to understand more broadly how glaciers and ice sheets evolve with climate.

Materials and Methods

To estimate the viscous stress exponent n and prefactor A, we couple the composite flow law presented in (9) with a model for ice temperature (36) and a model for steady-state grain size (37) using laboratory and observationally constrained activation energy values. The composite flow law explicitly represents multiple ice deformation mechanisms and is dependent upon the applied stress, the ice temperature, and the grain size, along with kinetic parameters (such as the activation energy and prefactor in the Arrhenius relation). Below, we discuss the models and relevant calculations.

Models for Estimating Rheology Parameters. The coupled model makes a few key assumptions. In estimating ice temperature and grain size, we first assume that both temperature and grain-size are in steady-state, a justified assumption based on the timescales to steady-state, as shown in (37). Therefore, the results shown here can be interpreted as constraining the mechanisms by which ice flows assuming a steady forcing. Secondly, the ice temperature and grain size models assume that the only advection of ice occurs vertically, and therefore horizontal (lateral and along-flow) advection is negligible.

Ice Temperature Model. To find ice temperature, we apply a one-dimensional thermomechanical model derived in (36). This model represents vertical advection and diffusion of heat, as well as a shear heating term. The shear heating term describes the irreversible dissipation of heat due to viscous deformation. Ice temperature is found by solving the following equation:

$$-\rho c_p a \frac{\partial T}{\partial z} = K \frac{\partial^2 T}{\partial z^2} + \tau_{ij}\dot{\epsilon}_{ij} \qquad [5]$$

where ρ is the mass density of ice, c_p is the specific heat capacity of ice, a is ice accumulation, T is ice temperature, z is the vertical coordinate (defined as being positive upwards and parallel to the gravity vector), K is thermal conductivity, τ_{ij} is the deviatoric stress tensor (we assume ice is incompressible), and $\dot{\epsilon}_{ij}$ is the strain-rate tensor. This equation is solved with the boundary conditions of $T = T_m$ at the boundary between cold and temperate ice, where T_m is the melting temperature, $T = T_s$ at the surface of the ice, where T_s is the surface temperature, and $-K\frac{\partial T}{\partial z} = 0$ at the cold-temperate boundary. The parameters used are found in Table 2 and the analytical solution to Equation 5 can be found in (36) along with futher details on the model.

Grain size model. To find grain size, we apply a one-dimensional steady-state grain size model derived in (37). This model computes the changes in grain size that occur due to recrystallization, a class of mechanisms that alter the size, shape, and orientation of ice grains. The model represents three mechanisms: normal grain growth, which grows grains in the absence of deformation to reduce surface energy (76), rotation recrystallization, which reduces grains in the presence of low-temperature deformation to reduce elastic strain energy (77), and migration recrystallization, which increases grain size in the presence of high-temperature deformation to reduce elastic strain energy (77, 78). Steady-state grain size is then found through the balances in surface and strain energies (37, 79) as:

$$d = \left[\frac{4kp^{-1}c\gamma\mu^2 + \tau^4 D^p (\frac{p}{2}) M}{8(1-\Theta)\tau\dot{\epsilon}\mu^2}\right]^{\frac{1}{1+p}} \qquad [6]$$

where k is the normal grain growth rate factor, p is the grain growth exponent, c represents the shape of grains, γ is grain boundary energy, μ is the shear modulus of ice, D is the characteristic length scale for strain energy, M is grain boundary mobility, and Θ is the partitioning between stored and thermal energy when ice deforms. The parameters we use are given in Table 3 and discussed in detail in (37).

Table 3. Parameters used in the grain size model. Low temperatures are those below 263 K and high temperatures are above 263 K.

Parameter	Value	Unit
k	$k_0 \exp -\left[\frac{Q_{gg}}{RT}\right]$	mm^p s^{-1}
k_0	11.4266	mm^p s^{-1}
Q_{gg}	40 at low temperatures, 100 at high temperatures	kJ mol^{-1}
p	9	-
c	6	-
γ	0.065	J m^{-2}
μ	3×10^9	Pa
D	0.3	m
M	$M_0 \exp -\left[\frac{Q_m}{RT}\right]$	m^2 s kg^{-1}
M_0	0.023	m^2 s kg^{-1}
Q_m	100 at low temperatures, 40 at high temperatures	kJ mol^{-1}
Θ	0.99	-

Updated flow law for use in ice-flow models. To simplify the incorporation of our upated flow law, we provide readers with the option to query our model results for values of n and A approapriate to their modeling needs. The results presented in the deformation maps of Figure 3 in the main text, are provided as an hdf5 file in the supplement and on Zenodo. Users may prefer to fit a spline to this surface for easy incorporation into their models.

Glacier stability model. To demonstrate the effect of n and A on marine ice sheet stability, we apply a model derived by (25), which builds on work by (24). This model estimates steady-state grounding line positions to analyze the stability of ice sheets. The glacier is laterally confined, with prescribed width $W = 40$ km and length of the ice shelf $L_s = 115$ km. The bed is defined as in (25), and a portion of the bed has a retrogade slope. Assuming a constant temperature of $T = 270$ K and grain size of 1 mm in all three cases, we estimate the steady-state grounding line flux q in the limit of strong buttressing (when $W << L_s$; (25) Equation 22a):

$$q = \frac{[\rho_i g(1-\rho_i/\rho_w)]^n A W^{n+1}}{(4^n C_w)^{1/(n+1)} W + \frac{1+n}{n} C_w L_s} h_g^{n+1} \qquad [7]$$

where ρ_i is the density of ice, ρ_w is the density of water, C_w is a parameter describing lateral shear stress, h_g is the ice thickness at the grounding line. The values of the parameters used are the same as described in (25). To find steady-states, Equation 7 must equal the total mass accumulation ax_g, where a represents the rate of snow accumulation. The grounding line flux intersects with the mass accumulation integrated over the grounded portion of the ice stream at the steady-state grounding line positions.

ACKNOWLEDGMENTS. The authors benefited greatly from discussions with Joanna Millstein, David Goldsby, Colin R. Meyer,

Jerome Neufeld. The authors also thank Marianne Haseloff for providing the code for the ice sheet stability model, and for providing the information for running the model. **Funding:** M.I.R. was supported by the School of Science Service Fellowship, Martin Fellowship, NSFGEO-NERC award 1853918, NEC Corporation Fund for Research in Computers and Communications, and the NOAA Climate Global Change postdoctoral fellowship. B.M. acknowledges funding from NSFGEO-NERC award 1853918, NSF-NERC award 1739031, and NEC Corporation Fund for Research in Computers and Communications. **Data and materials availability:** The source code for the model presented in this study are openly available at https://github.com/megr090/DeformationMechanisms. No new data were produced for this study, and data used in this study are publicly available through their respective publications.

1. B Fox-Kemper, et al., Ocean, Cryosphere and Sea Level Change. *Clim. Chang. 2021: The Phys. Sci. Basis. Contribution Work. Group I to Sixth Assess. Rep. Intergov. Panel on Clim. Chang. Basis. Contribution Work. Group I to Sixth Assess. Rep. Intergover* **2018**, 1–257 (2021).
2. E Rignot, J Mouginot, B Scheuchl, Ice Flow of the Antarctic Ice Sheet. *Science* **333**, 1427–1431 (2011).
3. AS Gardner, et al., Increased West Antarctic and unchanged East Antarctic ice discharge over the last 7 years. *The Cryosphere* **12**, 521–547 (2018).
4. J Mouginot, E Rignot, B Scheuchl, Continent-Wide, Interferometric SAR Phase, Mapping of Antarctic Ice Velocity. *Geophys. Res. Lett.* **46**, 9710–9718 (2019).
5. J De Rydt, R Reese, FS Paolo, GH Gudmundsson, Drivers of Pine Island Glacier speed-up between 1996 and 2016. *The Cryosphere* **15**, 113–132 (2021).
6. KM Cuffey, Manifestations of ice microphysical processes at the scale of whole ice sheets Manifestations of ice microphysical processes at the scale of whole ice sheets in *Glacier Science and Environmental Change*, ed. PG Knight. (Blackwell Science Ltd), pp. 290–300 (2006).
7. M Mellor, R Testa, Creep of Ice under Low Stress. *J. Glaciol.* **8**, 147–152 (1969).
8. DL Goldsby, DL Kohlstedt, Flow of ice by Dislocation, Grain Boundary Sliding, and Diffusion Processes. *Lunar Planet. Sci.* (1997).
9. DL Goldsby, DL Kohlstedt, Superplastic deformation of ice: Experimental observations. *J. Geophys. Res. Solid Earth* **106**, 11017–11030 (2001).
10. W Durham, L Stern, Rheological Properties of Water Ice - Applications to Satellites of the Outer Planets. *Annu. Rev. Earth Planet. Sci.* **29**, 295–330 (2001).
11. J Glen, The creep of polycrystalline ice. *Proc. Royal Soc. London. Ser. A. Math. Phys. Sci.* **228**, 519–538 (1955).
12. RH Thomas, The Creep of Ice Shelves: Interpretation of Observed Behaviour. *J. Glaciol.* **12**, 55–70 (1973).
13. K Jezek, R Alley, Thomas, Rheology of Glacier Ice. *Science* **227**, 1335–1337 (1985).
14. W Budd, T Jacka, A review of ice rheology for ice sheet modelling. *Cold Reg. Sci. Technol.* **16**, 107–144 (1989).
15. K Cuffey, W Paterson, *The Physics of Glaciers*. (Elsevier), Fourth edition, (2010).
16. E Larour, Rheology of the Ronne Ice Shelf, Antarctica, inferred from satellite radar interferometry data using an inverse control method. *Geophys. Res. Lett.* **32**, L05503 (2005).
17. P Barnes, D Tabor, JCF Walker, The friction and creep of polycrystalline ice. *Proc. Royal Soc. London. A. Math. Phys. Sci.* **324**, 127–155 (1971).
18. CJC Adams, NR Iverson, C Helanow, LK Zoet, CE Bate, Softening of Temperate Ice by Interstitial Water. *Front. Earth Sci.* **9**, 1–11 (2021).
19. J Nye, The distribution of stress and velocity in glaciers and ice-sheets. *Proc. Royal Soc. London. Ser. A. Math. Phys. Sci.* **239**, 113–133 (1957).
20. F Gillet-Chaulet, RC Hindmarsh, HF Corr, EC King, A Jenkins, In-situ quantification of ice rheology and direct measurement of the Raymond Effect at Summit, Greenland using a phase-sensitive radar. *Geophys. Res. Lett.* **38**, 1–7 (2011).
21. PD Bons, et al., Greenland Ice Sheet: Higher Nonlinearity of Ice Flow Significantly Reduces Estimated Basal Motion. *Geophys. Res. Lett.* **45**, 6542–6548 (2018).
22. JD Millstein, BM Minchew, SS Pegler, Ice viscosity is more sensitive to stress than commonly assumed. *Commun. Earth Environ.* **3**, 1–7 (2022).
23. V Rommelaere, DR Macayeal, Large-scale rheology of the Ross Ice Shelf, Antarctica, computed by a control method. *Annals Glaciol.* pp. 43–48 (1997).
24. C Schoof, Ice sheet grounding line dynamics: Steady states, stability, and hysteresis. *J. Geophys. Res.* **112**, F03S28 (2007).
25. M Haseloff, OV Sergienko, Effects of calving and submarine melting on steady states and stability of buttressed marine ice sheets. *J. Glaciol.* pp. 1–18 (2022).
26. M Zeitz, A Levermann, R Winkelmann, Sensitivity of ice loss to uncertainty in flow law parameters in an idealized one-dimensional geometry. *Cryosphere* **14**, 3537–3550 (2020).
27. J Weertman, Stability of the Junction of an Ice Sheet and an Ice Shelf. *J. Glaciol.* **13**, 3–11 (1974).
28. I Joughin, BE Smith, B Medley, Marine Ice Sheet Collapse Potentially Under Way for the Thwaites Glacier Basin, West Antarctica. *Science* **344**, 735–738 (2014).
29. D Goldsby, D Kohlstedt, Grain boundary sliding in fine-grained Ice I. *Scripta Materialia* **37**, 1399–1406 (1997).
30. P Pimienta, P Duval, Rate Controlling Processes in the Creep of Polar Glacier Ice. *Le J. de Physique Colloques* **48**, C1–243–C1–248 (1987).
31. M Montagnat, P Duval, Rate controlling processes in the creep of polar ice, influence of grain boundary migration associated with recrystallization. *Earth Planet. Sci. Lett.* **183**, 179–186 (2000).
32. P Duval, M Montagnat, Comment on "Superplastic deformation of ice: Experimental observations" by D. L. Goldsby and D. L. Kohlstedt. *J. Geophys. Res. Solid Earth* **107**, ECV 4–1–ECV 4–2 (2002).
33. MF Ashby, A first report on deformation-mechanism maps. *Acta Metall.* **20**, 887–897 (1972).
34. HJ Frost, M Ashby, *Deformation-Mechanism Maps: The Plasticity and Creep of Metals and Ceramics*. (Pergamon Press Ltd.), (1982).
35. JP Poirier, *Creep of Crystals: High-temperature deformation processes in metals, ceramics, and minerals*. (Cambridge University Press), (1985).
36. CR Meyer, BM Minchew, Temperate ice in the shear margins of the Antarctic Ice Sheet: Controlling processes and preliminary locations. *Earth Planet. Sci. Lett.* **498**, 17–26 (2018).
37. M Ranganathan, B Minchew, CR Meyer, M Peč, Recrystallization of ice enhances the creep and vulnerability to fracture of ice shelves. *Earth Planet. Sci. Lett.* **576**, 117219 (2021).
38. M Ranganathan, B Minchew, CR Meyer, GH Gudmundsson, A new approach to inferring basal drag and ice rheology in ice streams, with applications to West Antarctic Ice Streams. *J. Glaciol.* **67**, 229–242 (2021).
39. M Ranganathan, Jw Barotta, CR Meyer, B Minchew, Meltwater generation in ice stream shear margins: case study in Antarctic ice streams. *Proc. Royal Soc. A: Math. Phys. Eng. Sci.* **479**, 1–27 (2023).
40. DR MacAyeal, RA Bindschadler, TA Scambos, Basal friction of Ice Stream E, West Antarctica. *J. Glaciol.* **41**, 247–262 (1995).
41. I Joughin, DR MacAyeal, S Tulaczyk, Basal shear stress of the Ross ice streams from control method inversions. *J. Geophys. Res. Solid Earth* **109**, n/a–n/a (2004).
42. M Morlighem, H Seroussi, E Larour, E Rignot, Inversion of basal friction in Antarctica using exact and incomplete adjoints of a higher-order model. *J. Geophys. Res. Earth Surf.* **118**, 1746–1753 (2013).
43. M Ranganathan, BM Minchew, The effect of uncertainties in creep activation energies on modeling ice flow and deformation. *EarthArXiv* (2022).
44. M Zeitz, R Winkelmann, A Levermann, Implications of flow law uncertainty for flow-driven ice-loss in Greenland under idealized warming pathways. *Preprint* pp. 1–21 (2021).
45. EJN Kuiper, et al., Using a composite flow law to model deformation in the NEEM deep ice core, Greenland-Part 2: The role of grain size and premelting on ice deformation at high homologous temperature. *Cryosphere* **14**, 2449–2467 (2020).
46. EC Pettit, ED Waddington, Ice flow at low deviatoric stress. *J. Glaciol.* **49**, 359–369 (2003).
47. CR Meyer, A Yehya, B Minchew, JR Rice, A Model for the Downstream Evolution of Temperate Ice and Subglacial Hydrology Along Ice Stream Shear Margins. *J. Geophys. Res. Earth Surf.* **123**, 1682–1698 (2018).
48. CF Raymond, Inversion of flow Measurements for Stress and Rheological Parameters in a Valley Glacier. *J. Glaciol.* **12**, 19–44 (1973).
49. WSB Paterson, Deformation within polar ice sheets: an analysis of the Byrd Station. *Cold Reg. Sci. Technol.* **8**, 165–179 (1983).
50. N Reeh, WS Paterson, Application of a flow model to the ice-divide region of Devon Island ice cap, Canada. *J. Glaciol.* **34**, 55–63 (1988).
51. RH Thomas, DR MacAyeal, CR Bentley, JL Clapp, The Creep of Ice, Geothermal Heat Flow, and Roosevelt Island, Antarctica. *J. Glaciol.* **25**, 47–60 (1980).
52. KM Cuffey, JL Kavanaugh, How nonlinear is the creep deformation of polar ice? A new field assessment. *Geology* **39**, 1027–1030 (2011).
53. M Morlighem, et al., Deep glacial troughs and stabilizing ridges unveiled beneath the margins of the Antarctic ice sheet. *Nat. Geosci.* **13**, 132–137 (2020).
54. IM Howat, C Porter, BE Smith, MJ Noh, P Morin, The Reference Elevation Model of Antarctica. *The Cryosphere* **13**, 665–674 (2019).
55. JM Van Wessem, et al., Improved representation of East Antarctic surface mass balance in a regional atmospheric climate model. *J. Glaciol.* **60**, 761–770 (2014).
56. BM Minchew, M Simons, B Riel, P Milillo, Tidally induced variations in vertical and horizontal motion on Rutford Ice Stream, West Antarctica, inferred from remotely sensed observations. *J. Geophys. Res. Earth Surf.* **122**, 167–190 (2017).
57. P Fretwell, et al., Bedmap2: improved ice bed, surface and thickness datasets for Antarctica. *The Cryosphere* **7**, 375–393 (2013).
58. HP Jacobson, CF Raymond, Thermal effects on the location of ice stream margins. *J. Geophys. Res. Solid Earth* **103**, 12111–12122 (1998).
59. WD Harrison, KA Echelmeyer, CF Larsen, Measurement of temperature in a margin of Ice Stream B, Antarctica: implications for margin migration and lateral drag. *J. Glaciol.* **44**, 615–624 (1998).
60. C Schoof, On the mechanics of ice-stream shear margins. *J. Glaciol.* **50**, 208–218 (2004).
61. J Suckale, JD Platt, T Perol, JR Rice, Deformation-induced melting in the margins of the West Antarctic ice streams. *J. Geophys. Res. Earth Surf.* **119**, 1004–1025 (2014).
62. P Hunter, C Meyer, B Minchew, M Haseloff, A Rempel, Thermal controls on ice stream shear margins. *J. Glaciol.* pp. 1–15 (2021).
63. P Duval, L Arnaud, O Brissaud, M Montagnat, S de la Chapelle, Deformation and recrystallization processes of ice from polar ice sheets. *Annals Glaciol.* **30**, 83–87 (2000).
64. MF Meier, Mode of flow of Saskatchewan Glacier, Alberta, Canada. *Geol. Surv. Prof. Pap.* **351**, 70 (1960).
65. SC Colbeck, RJ Evans, A Flow Law for Temperate Glacier Ice. *J. Glaciol.* **12**, 71–86 (1973).
66. TG Langdon, The physics of superplastic deformation. *Mater. Sci. Eng. A* **137**, 1–11 (1991).
67. L Lliboutry, The Dynamics of Temperature Glaciers from the Detailed Viewpoint. *J. Glaciol.* **56** (1969).
68. GD Smith, LW Morland, Viscous relations for the steady creep of polycrystalline ice. *Cold Reg. Sci. Technol.* **5**, 141–150 (1981).
69. M Montagnat, P Duval, Dislocations in ice and deformation mechanisms: From single crystals to polar ice. *Defect Diffusion Forum* **229**, 43–54 (2004).
70. CJ Wilson, Y Zhang, Development of microstructure in the high-temperature deformation of ice. *Annals Glaciol.* **23**, 293–302 (1996).
71. EC Pettit, T Thorsteinsson, HP Jacobson, ED Waddington, The role of crystal fabric in flow near an ice divide. *J. Glaciol.* **53**, 277–288 (2007).
72. Y Ma, et al., Enhancement factors for grounded ice and ice shelves inferred from an anisotropic ice-flow model. *J. Glaciol.* **56**, 805–812 (2010).
73. T Chauve, M Montagnat, P Vacher, Strain field evolution during dynamic recrystallization nucleation; A case study on ice. *Acta Materialia* **101**, 116–124 (2015).

74. BM Minchew, CR Meyer, AA Robel, GH Gudmundsson, M Simons, Processes controlling the downstream evolution of ice rheology in glacier shear margins: case study on Rutford Ice Stream, West Antarctica. *J. Glaciol.* **64**, 583–594 (2018).
75. FS Graham, M Morlighem, RC Warner, A Treverrow, Implementing an empirical scalar constitutive relation for ice with flow-induced polycrystalline anisotropy in large-scale ice sheet models. *The Cryosphere* **12**, 1047–1067 (2018).
76. R Alley, J Perepezko, C Bentley, Grain Growth in Polar Ice: I. Theory. *J. Glaciol.* **32**, 425–433 (1986).
77. P Duval, O Castelnau, Dynamic recrystallization of ice in polar ice sheets. *J. de Physique IV* **5**, 197–205 (1995).
78. P Duval, MF Ashby, I Anderman, Rate-controlling processes in the creep of polycrystalline ice. *J. Phys. Chem.* **87**, 4066–4074 (1983).
79. NJ Austin, B Evans, Paleowattmeters: A scaling relation for dynamically recrystallized grain size. *Geology* **35**, 343 (2007).